

UNCERTAINTY QUANTIFICATION OF INCLUSION BOUNDARIES IN THE CONTEXT OF X-RAY TOMOGRAPHY*

BABAK MABOUDI AFKHAM[†], YIQIU DONG[†], AND PER CHRISTIAN HANSEN[†]

Abstract. In this work, we describe a Bayesian framework for the X-ray computed tomography (CT) problem in an infinite-dimensional setting. We consider reconstructing piecewise smooth fields with discontinuities where the interface between regions is not known. Furthermore, we quantify the uncertainty in the prediction. Directly detecting the discontinuities, instead of reconstructing the entire image, drastically reduces the dimension of the problem. Therefore, the posterior distribution can be approximated with a relatively small number of samples. We show that our method provides an excellent platform for challenging X-ray CT scenarios (e.g. in case of noisy data, limited angle, or sparse angle imaging). We investigate the accuracy and the efficiency of our method on synthetic data. Furthermore, we apply the method to the real-world data, tomographic X-ray data of a lotus root filled with attenuating objects. The numerical results indicate that our method provides an accurate method in detecting boundaries between piecewise smooth regions and quantifies the uncertainty in the prediction, in the context of X-ray CT.

Key words. X-ray CT, Bayesian framework, inverse problems, Whittle-Matérn field

AMS subject classifications. 60G10, 60G15, 60G50, 60G60, 60J20, 28-08, 46B99, 65C05, 65C20, 65C40

1. Introduction. Computed tomography (CT) imaging is the task of reconstructing a positive field (attenuation field or image) from a finite number of projections (e.g. X-ray images). CT reconstruction is often formulated as an inverse problem [24]. *Filtered back-projection* [29] is a classic reconstruction approach to solve this inverse problem for some CT settings. However, imaging challenges, e.g. noise, sparse angle imaging (to reduce the amount of harmful radiation), or limited angle imaging (to avoid obstacles in the imaging site or due to application set-up e.g. in mammography), compromise the quality of the reconstructed image. Therefore, finding alternative approaches for CT reconstruction has attracted attention in the past few decades [11, 6, 32, 43, 39, 38].

In many CT reconstruction methods, such as algebraic iterative methods and regularization methods [20], the goal is to identify objects in the image with approximately homogeneous attenuation coefficient distinct from the background attenuation [13, 17, 18, 46]. Therefore, CT reconstruction is often followed by an image segmentation step to partition the image into piecewise smooth/constant regions. The boundaries between such regions often carry valuable information [44]. Error propagation from reconstruction to segmentation, due to concatenation of such methods, can introduce artifacts in the reconstruction. Such effects are also amplified in case of noisy or incomplete data.

To avoid such artifacts many methods attempt to combine the reconstruction and the segmentation (and subsequently boundary extraction) steps. One common approach is to describe the images as a level set of a smooth functions, e.g. see [6, 26, 32, 2, 47, 48, 43] for some selected examples. Another common approach is to construct a deforming/parametric curve which evolves to fit the boundaries between partitions, e.g. see [11, 39, 40, 38] as a non-exhaustive selection. Large parameter

*Submitted to the editors DATE.

Funding: This project is supported by The Villum Foundation (grant no. 25893).

[†]Department of Applied Mathematics and Computer Science, Technical University of Denmark, Lyngby, Denmark (bmaaf@dtu.dk, yido@dtu.dk, pcha@dtu.dk).

spaces, dependency on discretization, noisy data, and limited angle imaging can be challenging for some of the mentioned methods. However, all the methods mentioned above lack the quantification of the uncertainties in the reconstructed/segmented images with respect to noisy/perturbed data. Uncertainty quantification could be particularly important in applications where images are used to determine the location and the size of objects. For example, in medical imaging, CT reconstruction is used to tracking the evolution of tumor boundaries over time and make treatment decisions.

A popular approach to characterize uncertainties for inverse problems is within the Bayesian framework. In this approach, all quantities of a model are represented as random variables. The solution to the inverse problem is then the probability distribution, *the posterior distribution*, of the quantity of interest after all given information (e.g. the *prior* belief in the model) is incorporated into the model. Qualities of the posterior distribution can then be interpreted as the degree of confidence in predicting the quantity of interest.

In the past decade, a formulation of a Bayesian inversion theory in an infinite dimensional setting has attracted attention, see [12] and the references therein. In this setting, model parameters are modeled as random functions rather than real-valued random variables. This provides a discretization-independent numerical platform for exploring the posterior distribution.

Infinite-dimensional Bayesian methods for tomography problems are not new. For recent works in the context of electrical impedance tomography (EIT), inverse scattering problem and other partial differential equation based inverse problems see [15, 14, 28, 5, 21, 16, 25] and the references therein. The underlying partial differential equation provides a natural platform (a Hilbert space) for the infinite-dimensional random variable to be well defined. Detailed analysis of these inverse problems in a Bayesian setting [12] shows that the solution (the posterior distribution) is well-defined and bounded under perturbations in data. Therefore, the Bayesian platform provides an alternative method to investigate the well-posedness of an inverse problem.

In the context of X-ray CT, the Bayesian method has been successfully applied. See e.g. but not limited to [41, 8, 43, 9, 7, 43] recent works. However, to the best knowledge of the authors, we still lack a well-established infinite-dimensional framework for the X-ray CT problem. We argue that the well-posedness results, mentioned above, can be naturally extended to the X-ray CT problem. This provides an excellent tool to evaluate and quantify the uncertainties in the reconstruction and segmentation of images.

In this paper, we provide a goal-oriented, infinite-dimensional Bayesian framework for the X-ray CT problem. We specifically look for objects/inclusions in an image with a homogeneous attenuation coefficient distinct from the background. The method consists of two stages: in the first stage, an approximate location of the object is identified. The second stage identifies the boundary of the object. Furthermore, we provide an uncertainty band around the boundary to quantify our reliability in the prediction of the boundary.

In the first stage, 2D Gaussian random fields [22] are used to describe images. Random fields are infinite-dimensional analogous to random variables. The correlation length parameter in this field controls our belief in how large or small the inclusions are in an image. Furthermore, the regularity parameter encodes the smoothness or roughness of the boundary of the inclusions. This provides an excellent modeling tool in the case of sparse and limited angle imaging where the missing information in data is filled with our belief in the overall size and roughness of the inclusions. The approximate location of inclusions is estimated from the posterior distribution of the

image.

In the second stage of the method, we use the star-shaped formulation [16] to represent the inclusions. This representation defines the inclusions by a center and a radial 1D Gaussian random field. This representation makes convergence properties of the method independent of imaging/discretization resolution. Furthermore, describing the inclusion with their boundaries (rather than their volume) reduces the dimensionality of the problem from finding a 2D image to a 1D boundary of a region. The reduced dimensionality significantly reduces the costs of numerical exploration of the posterior distribution. We show that the second stage of the method can be parallelized with respect to the number of inclusions, providing excellent computational efficiency.

This paper is organized as follows: In Section 2 we formulate the X-ray CT and introduce the Radon transform. The infinite dimensional Bayesian framework to inverse problems is presented in Section 3. Here, we introduce the Matérn-Whittle random field and construct the log-Gaussian, level set and the star-shaped priors. We introduce the posterior and discuss the well-posedness of the posterior distribution. In Section 4 we introduce the two stage method in identifying inclusion boundaries. We evaluate the performance of the method for simulated images in Section 5 for single and multiple inclusions, as well as, in sparse and limited angle imaging settings. In addition, we show the performance of the method on a real CT-scan of a tomographic X-ray data of a lotus root slice filled with different chemical elements [3]. We present conclusive remarks in Section 6.

2. Radon Transform and Forward Model. Tomography, or slice/volume imaging, comprises methods in reconstructing the internal structure of an object from external measurements.

In X-ray computed tomography, X-ray beams are casted through an object which interacts with the matter within the object. Measurement comprises collecting the affected beams on sensors placed on the other side of the object [37].

A common approach in modeling X-ray interaction with an object is described by line integrals over a density field. Let $D \subset \mathbb{R}^2$ be a bounded region with Lipschitz boundary. We denote $0 < \alpha \in L^2(D)$ to be a density field defined on D . This field, e.g., represents the attenuation of X-ray beams [37]. A measurement can then be described by the line integral

$$(2.1) \quad R_{\theta,s}[\alpha] := \int_{L_{\theta,s}} \alpha(x,y) \, dl.$$

Here, $s \in [-1, 1]$ parameterizes points on the line L_θ^\perp passing through the origin and making the angle $\theta \in [0, \theta_{\max})$, $\theta_{\max} \leq \pi$, with the x -axis. Furthermore, $L_{\theta,s}$ is the perpendicular line to L_θ^\perp crossing it at point s , and dl is an infinitesimally small length on $L_{\theta,s}$. We assume that α has a compact support such that the integration in (2.1) is carried over a finite section of $L_{\theta,s}$.

Note that $R_{\cdot,\cdot}$ can be viewed as a linear functional from lines in \mathbb{R}^2 to \mathbb{R} in which case it is referred to as the *Radon transform*. The simplest set of measurement lines to carry line integral (2.1) are a finite set of equidistant parallel lines perpendicular to L_θ^\perp . This setup is referred to as the *parallel-beam geometry*. The collected measurements of this type is commonly referred to as a *sinogram*. An illustration of Radon transform for a parallel-beam geometry is presented in Figure 1.

We discretize θ into N_θ angles and s into N_s detector pixels to construct $N := N_\theta \times N_s$ measurements. We define an observation vector $y(\alpha) \in \mathbb{R}^N$ to contain

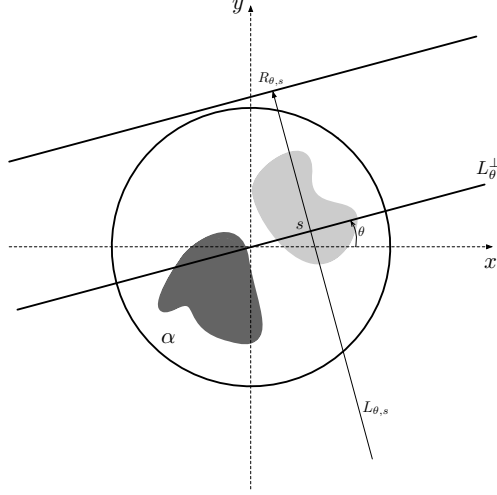


FIG. 1. Radon transform for parallel-beam geometry. Here, the circle represents the domain D , α is the attenuation coefficient in D , and the gray areas represent inclusions.

elements of noisy measurement of type

$$(2.2) \quad y_{i,j}(\alpha) = R_{\theta_i,s_j}\alpha + \varepsilon_{i,j}, \quad i = 1, \dots, N_\theta, \quad j = 1, \dots, N_s,$$

where $\varepsilon_{i,j}$ are independent and identically distributed (i.i.d.) following $\mathcal{N}(0, \sigma_n^2)$, for some $\sigma_n > 0$. Note that, in general, noise in CT data is non-Gaussian. The choice of observation noise in (2.2) is an approximation. Representing (2.2) in vector form we obtain

$$(2.3) \quad y(\alpha) = G(\alpha) + \varepsilon.$$

Here, $G : L^2(D) \rightarrow \mathbb{R}^N$ contains line-integrals R_{θ_j,s_j} referred to as the *forward map* and $\varepsilon \sim \mathcal{N}(\mathbf{0}, \Sigma_n)$, with $\Sigma_n = \text{diag}(\sigma_n^2, \dots, \sigma_n^2)$. Note that since R_{θ_j,s_j} is linear then G is locally Lipschitz.

The task of finding α from $y(\alpha)$ forms an inverse problem. This inverse problem is severely under-determined since α is infinite dimensional and y is finite dimensional.

In many tomography applications we are not interested in reconstructing the entire α , but to extract some information within α , e.g. location of discontinuities in α . In this paper we are particularly interested in finding and quantifying the uncertainty of discontinuities, inclusions, in α . Such discontinuities can be parameterized with a significantly lower dimensionality than α .

A common approach to detect discontinuities in a reconstructed α is done using a post-processing step. Reconstruction error can affect the quality of this detection. One approach to address such challenges is to directly detect discontinuities in α [11], without reconstructing the entire field. Direct extraction of information from the observation y , on one hand, drastically reduces the dimensionality and, on the other hand, enhances the quality of predictions.

In this article, we take a Bayesian approach in representing the tomography inverse problem. Severe under-determination of the inverse problem is regularized by a prior knowledge/assumption on α in the form of a probability distribution. Applying the Bayes' theorem to combine the prior distribution with the forward map G results in a posterior distribution which represents the solution to the inverse problem.

3. Bayesian Modeling. In this section we introduce various prior modeling techniques to construct a density field α . We then introduce Bayes' theorem to construct the posterior distribution.

3.1. Prior Modeling. Let $(\Omega, \mathcal{A}, \mathbb{P})$ be a complete probability space with Ω a measurable space, \mathcal{A} a σ -algebra defined on Ω and \mathbb{P} a probability measure. Furthermore let $(H, \langle \cdot, \cdot \rangle)$ be a Hilbert space. See [22] for further information on a probability space. A random element $\xi \in H$ is called an H -valued Gaussian random variable if $\langle \xi, \zeta \rangle$, for all $\zeta \in H$, is a real-valued Gaussian random variable, i.e. measurable function on the probability space $(\Omega, \mathcal{A}, \mathbb{P})$.

THEOREM 3.1. [22] *Let ξ be an H -valued Gaussian random variable. Then we can find $m \in H$, mean function, and a symmetric, non-negative and trace-class linear operator $Q : H \rightarrow H$, covariance operator, such that*

$$(3.1a) \quad \langle m, \zeta \rangle = \mathbb{E} \langle \xi, \zeta \rangle, \quad \forall \zeta \in H,$$

$$(3.1b) \quad \langle Q\zeta, \eta \rangle = \mathbb{E} \langle \xi - m, \zeta \rangle \langle \xi - m, \eta \rangle, \quad \forall \zeta, \eta \in H,$$

where \mathbb{E} represents expectation. We write $\xi \sim \mathcal{N}(m, Q)$ and say ξ is Gaussian with measure $\mathbb{P} \circ \xi^{-1}$.

THEOREM 3.2. [19] *Let $m \in H$ and $Q : H \rightarrow H$ be a symmetric, non-negative and trace-class linear covariance operator. Furthermore let $\{e_i\}_{i \in \mathbb{N}}$ be eigenfunctions of Q and $\{\lambda_i\}_{i \in \mathbb{N}}$ be eigenvalues of Q sorted in decreasing order. An H -valued random variable ξ is a Gaussian random variable distributed according $\mathcal{N}(m, Q)$ if and only if*

$$(3.2) \quad \xi = m + \sum_{i \in \mathbb{N}} \sqrt{\lambda_i} \beta_i e_i,$$

where $\{\beta_i\}_{i \in \mathbb{N}}$ is a sequence of i.i.d. real-valued random variables with distribution $\mathcal{N}(0, 1)$. The expansion in (3.2) is referred to as the Karhunen-Loève (KL) expansion of ξ .

Remark 3.3. In case all random variables are Gaussian random variables, we can construct a probability measure on H using push-forward notation $\mu_0 = \xi_*(\mathbb{P})$. Therefore, $(H, \mathcal{B}(H), \mu_0)$, with $\mathcal{B}(H)$ the Borel σ -algebra, forms a probability space. We refer to μ_0 as the *prior measure*.

Theorem 3.2 indicates how we can construct random functions on a Hilbert space H using a covariance operator Q . We can approximate the sum in (3.2) by truncating it after N_{KL} terms. We refer the reader to [22, 19] for convergence properties of the KL expansion.

In the following subsection we introduce a family of covariance operators that we can use to construct Gaussian random functions according to (3.2).

3.1.1. Matérn-Whittle Covariance. A widely used family of covariance operators are the Matérn-Whittle covariance operators [33, 22, 35, 49] which allows control over regularity, amplitude and correlation length of samples. Here we briefly introduce this covariance operator but we refer the reader to [Appendix A](#) for a deeper discussion.

A simplified Matérn-Whittle covariance operator [25] is given by

$$(3.3) \quad Q_{\gamma, \tau} = (\tau^2 I - \Delta)^{-\gamma}.$$

Here, $\tau = 1/\ell > 0$ controls the correlation length and $\gamma = \nu + 1$ is the smoothness parameter (see [27] for more detail). For the covariance operator (3.3) to be well

defined we need to impose proper boundary conditions. See [35] for more detail on types of boundary conditions.

We note that in one dimension, i.e. when $D \subset \mathbb{R}$, and for $\tau = 1$ the zero-mean Gaussian random variable ξ distributed according to the covariance $Q_{\gamma,1}$ takes the form

$$(3.4) \quad \xi(x) = c \sum_{i \in \mathbb{N}} \left(\frac{1}{k} \right)^\gamma (\xi_i^1 \sin(kx) + \xi_i^1 \cos(kx)),$$

for some constant $c > 0$. Here, $\xi_i^1, \xi_i^2 \sim \mathcal{N}(0, 1)$ are real Gaussian random variables. This type of Gaussian random variables will be used in later sections to model the boundaries of inclusions.

3.2. Likelihood. In this section we apply a nonlinear transformation on Gaussian random variables to construct various types of images α . The level set and the star-shaped fields are used to construct piecewise constant images. Later in the section we discuss how to use these fields to construct a likelihood function.

3.2.1. Level Set Parameterization. Let ξ be an H -valued Gaussian random variable and take $c \in \mathbb{R}$. Define $D_i \subset D$, for $i = 1, 2$ as

$$(3.5) \quad D_1 := \{x \in D \mid \xi(x) < 0\}, \quad D_2 := D \setminus D_1.$$

We define the level set mapping $F_{\text{ls}} : H \rightarrow L^p(D)$, with $2 \leq p < \infty$, as

$$(3.6) \quad F_{\text{ls}}[\xi](x) = a^- \mathbb{1}_{D_1}(x) + a^+ \mathbb{1}_{D_2}(x),$$

where $\mathbb{1}_{D_i}(x)$, for $i = 1, 2$, is the indicator function and $0 < a^- < a^+$. We define $D^0 = \overline{D_1} \cap \overline{D_2}$ which contains the points of discontinuity. Throughout this paper we assume that $m(D^0) = 0$ where m is the Lebesgue measure defined on \overline{D} . This assumption is to ensure that the boundary of the inclusions has indeed a lower dimensionality than the image α . We refer the reader to [23] for more detail.

Remark 3.4. It is shown in [23] that the assumption $m(D^0) = 0$ is sufficient for F_{ls} to be continuous. This means if $\{\xi^\epsilon\}_{\epsilon > 0}$ is a sequence of functions such that for any $x \in D$

$$(3.7) \quad \xi(x) - \epsilon \leq \xi^\epsilon \leq \xi(x) + \epsilon.$$

Then $\|F_{\text{ls}}[\xi^\epsilon] - F_{\text{ls}}[\xi]\|_{L^p(D)} \rightarrow 0$, μ_0 -almost surely.

3.2.2. Star-Shaped Parameterization. Let $H = \mathbf{T}([0, 2\pi)) \subset L^2([0, 2\pi))$ where \mathbf{T} is the one dimensional Torus. Furthermore, define $\vartheta : D \rightarrow [0, 2\pi)$ be the continuous map from Cartesian coordinates to the angular component of polar coordinates. Define *star-shaped inclusions* $D_i \subset D$, for $i = 1, \dots, N_{\text{inc}}$, as

$$(3.8) \quad D_i(\xi_i, c_i) := \{x \in D \mid \|x - c_i\|_2 < F_{\text{LG}}(\xi_i(\vartheta(x - c_i)))\},$$

where

$$(3.9) \quad F_{\text{LG}}[\xi] = \exp(\xi)$$

defines the *log-Gaussian* field $F_{\text{LG}} : H \rightarrow L^2(D)$ in order to construct an image with positive attenuation. Here ξ is an H -valued Gaussian random variable. Since D is

bounded, then F_{LG} is almost surely a continuous map. In addition, $\|\cdot\|_2$ is the Euclidean norm and $c_i \in D$ for $i = 1, \dots, N_{\text{inc}}$ are independent stochastic centers of inclusions. Note that c_i and ξ_i are not necessarily i.i.d. Let $D_0 := (D_1 \cup \dots \cup D_{N_{\text{inc}}})^C$. We define the star-shaped mapping $F_{\text{star}} : H^{N_{\text{inc}}} \times \mathbb{R}^{2N_{\text{inc}}} \rightarrow L^p(D)$, with $2 \leq p < \infty$, as

$$(3.10) \quad F_{\text{star}}[(\xi_1, c_1), \dots, (\xi_{N_{\text{inc}}}, c_{N_{\text{inc}}})](x) = a^- \mathbb{1}_{D_0}(x) + \sum_{i=1}^{N_{\text{inc}}} a^+ \mathbb{1}_{D_i}(x),$$

where $a^- < a^+ \in \mathbb{R}^+$ and we refer to a^+ as the inclusion intensity. We may write the left hand side of (3.10) as $F_{\text{star}}[(\xi_i, c_i)]$ for simplicity. The following assumptions are considered when drawing samples of ξ_i and c_i :

- (I) D_i , for $i = 1, \dots, N_{\text{inc}}$ are disjoint.
- (II) $\|x - y\|_2 > d_{\min}^{\partial D}$, for all $x \in D_1 \cup \dots \cup D_{N_{\text{inc}}}$ and $y \in \partial D$ the boundary of D . This insures all inclusions are away from the boundary of D .
- (III) $\|x - y\|_2 > d_{\min}^D$, for all $x \in D_i$ and $y \in D_j$ for $i \neq j$ and $i, j \neq 0$. This insures that the inclusions are well separated.

Remark 3.5. It is shown in [16] that when $N_{\text{inc}} = 1$ and ξ_1 is Lipschitz continuous (e.g. $\gamma > 1$ in (3.3)) then F_{star} is a continuous mapping. This means if $\{\xi_1^\epsilon\}_{\epsilon>0}$ and $\{c_1^\epsilon\}_{\epsilon>0}$ are sequences of H -valued random variables and sequence of points in D , respectively, such that $\|\xi_1 - \xi_1^\epsilon\|_\infty \rightarrow 0$ and $\|c_1^\epsilon - c_1\|_2 \rightarrow 0$, then $F_{\text{star}}[(\xi_i^\epsilon, c_i^\epsilon)] \rightarrow F_{\text{star}}[(\xi_i, c_i)]$ in measure. When $N_{\text{inc}} > 1$, assumptions (I)-(III) ensures that we can divide D into subregions with only single inclusions.

The background attenuation $a^- \mathbb{1}_{D_0}$ in (3.10) is constant. However, in many applications a^- varies smoothly in the domain. To account this variation, we modify (3.10) to

$$(3.11) \quad F_{\text{star}}^{\text{noisy}}[\xi_0, (\xi_i, c_i)](x) = F_{LG}[\xi_0](x) \mathbb{1}_{D_1}(x) + \sum_{i=1}^{N_{\text{inc}}} a^+ \mathbb{1}_{D_i}(x).$$

We distinguish between the noise term ε in (2.3) and the variation in the background $F_{LG}[\xi_0](x)$ in our model. The latter often accounts for experiment's systematic error while the former noise models the measurement error.

We need to specify a prior measure μ_0 for (ξ_i, c_i) . We assume that ξ_i and c_i , for $i \leq N_{\text{inc}}$, are independent. We define $\mu_0 = \mu_0^1 \otimes \mu_0^2$, where μ_0^1 is a Gaussian measure on $H^{N_{\text{inc}}}$ and μ_0^2 is a measure on $\mathbb{R}^{2 \times N_{\text{inc}}}$ (e.g. Lebesgue measure). Note that since ξ_i and c_i , for $i = 1, \dots, N_{\text{inc}}$ are independent μ_0^1 and μ_0^2 are factorized further into simpler measures as $\mu_0^1 = \mu_0^{1,1} \otimes \mu_0^{1,N_{\text{inc}}}$ and $\mu_0^2 = \mu_0^{2,1} \otimes \mu_0^{2,N_{\text{inc}}}$. We define the random variable $\xi = (\xi_i, c_i)$ and equip the space $H^{N_{\text{inc}}} \times \mathbb{R}^{2N_{\text{inc}}}$ with the norm $\|(\xi_i, c_i)\|_X := \sum_i \|\xi_i\|_H + \sum_i \|c_i\|_2$.

3.2.3. Likelihood Function. In Subsection 3.1 we defined the probability space $(H^i, \mathcal{B}(H^i), \mu_0)$, $i = 0, \dots, N_{\text{inc}}$, with $H^0 = L^2(D)$ and $H^i = L^2(\mathbf{T})$. Let ξ_i , $i = 0, \dots, N_{\text{inc}}$ be an H^i -valued random variables¹ and c_i , $i = 1, \dots, N_{\text{inc}}$, be random centers, distributed according μ_0 . We define the image α , in (2.2), to be $\alpha(\xi_0) = F_{\text{ls}}[\xi_0]$ or $\alpha((\xi_i, c_i)) := F_{\text{star}}[(\xi_i, c_i)]$. In the rest of this section we construct the Bayesian likelihood and the posterior using the star-shaped field. The Bayesian formulation

¹the superscript i in H^i indicates the index of the space corresponding to the random variable ξ^i . This should not be confused with the differentiability order of the Hilbert space.

and the results regarding the level set field follows immediately letting the center component c_i be constant. We refer the reader to [16] for a detailed discussion.

Recall that the noise ε is distributed according to $\varepsilon \sim \mathcal{N}(\mathbf{0}, \Sigma_n)$. We define the joint random variable $(\alpha, \varepsilon) \in H \times \mathbb{R}^N$. The *log-likelihood* function $\Phi : H^{N_{\text{inc}}+1} \times \mathbb{R}^{2N_{\text{inc}}} \times \mathbb{R}^N \rightarrow \mathbb{R}$ is formulated as the least squares distance

$$(3.12) \quad \Phi(\xi; y) = \frac{1}{2} \|y - \mathcal{G}((\xi_i, c_i))\|_{\Sigma_n}^2.$$

Here, $\mathcal{G} = G \circ F_{\text{star}}$, and $\|\cdot\|_{\Sigma_n} = \|\Sigma_n^{-1/2} \cdot\|_2$. The log-likelihood function (3.12) for the tomography problem (i.e. $\mathcal{G} = G \circ F_{\text{star}}$) satisfies the following assumptions:

- (i) For all $y \in \mathbb{R}^N$ with $\|y\|_{\Sigma_n} < r$, for a fixed $0 < r < \infty$, we can find $K(r) > 0$ such that

$$(3.13) \quad 0 \leq \Phi((\xi_i, c_i); y) < K(r), \quad \forall \xi \in H.$$

- (ii) For a fixed observation $y \in \mathbb{R}^N$, $\Phi(\cdot, y) : H \rightarrow \mathbb{R}$ is μ_0 -almost surely continuous.
- (iii) for two separate observations $y_1, y_2 \in \mathbb{R}^N$ with $\|y_1\|_{\Sigma_n}, \|y_2\|_{\Sigma_n} \leq r$, for a fixed $r > 0$ we have

$$(3.14) \quad |\Phi((\xi_i, c_i); y_1) - \Phi((\xi_i, c_i); y_2)| \leq C \|y_1 - y_2\|_{\Sigma_n}, \forall \xi_i \in H^i, c_i \in D.$$

Assumption (i) follows from the fact that F_{star} and F_{ls} are bounded by definition and G is a linear operator. We discussed in Subsections 3.2.1 and 3.2.2 that F_{star} and F_{ls} are both μ_0 -almost surely continuous. Since \mathcal{G} is a composition of μ_0 -almost surely continuous mappings then assumption (ii) is verified. Finally, the triangle inequality shown in assumption (iii) is true for all least-squares-type log-likelihood functions.

3.3. Posterior Distribution. In this section we present the Bayes' theorem to connect the prior measure with the likelihood function and construct the posterior measure μ^y .

THEOREM 3.6. [12] *Let Φ be the log-likelihood defined (3.12) satisfying assumptions (i)-(iii) in Subsection 3.2.3 and μ_0 be the prior measure defined on $(H, \mathcal{B}(D))$. Then there is a posterior measure μ^y absolutely continuous with respect to μ_0 , i.e. $\mu^y \ll \mu_0$, and is defined through the Radon-Nikodym derivative [22]*

$$(3.15) \quad \frac{d\mu^y}{d\mu^0} = \frac{1}{Z} \exp(-\Phi((\xi_i, c_i); y)),$$

where Z is the normalization constant and for y -almost surely

$$(3.16) \quad Z := \int_H \exp(-\Phi((\xi_i, c_i); y)) \mu_0(d\xi) > 0.$$

The well-posedness of the tomography inverse problem (2.3) for both nonlinear maps F_{ls} and F_{star} are discussed in Appendix B. In the next section we combine these two nonlinear maps in an algorithm to both identify the location and boundaries of inclusions in an image α .

4. 2-Stage Method for Detecting Inclusion Boundaries. In Section 3 we formulate the Bayesian approach for modeling the inverse tomography problem. In Subsection 3.2 present multiple prior models that can be used in constructing a posterior distribution.

In this section we provide a 2-stage method in detecting the location of inclusions in an image and also predict the boundary of the inclusions. In the first stage we use the level set prior (3.6) to construct a posterior and use the mean to predict the locations of inclusions. In an intermediate step, we assign approximate centers to the predicted inclusions from the posterior mean. In the second stage of the method we use the star-shape prior to predict the boundary of the inclusions.

We remind the reader that the star-shaped prior for multiple inclusions with an unknown center can be used to construct a posterior. However, constructing a sampling method for such posterior is challenging (e.g. the Metropolis-within-Gibbs-type method can result in highly correlated samples and increased computational cost, see [36]). The first stage of the method is to ensure that we can decompose the images into regions containing a single inclusion. Remark 3.5 then guarantees that we can converge to the right solution for each individual inclusion. This decomposition also allows parallel computation, with respect to the number of inclusions, for exploring the posterior.

4.1. Stage One: Estimating Centers of Inclusions. In this section we construct the posterior measure μ^y in (3.15) using the Matérn Covariance (3.3) and the level set map F_{ls} introduced in (3.6).

We assume that the correlation length parameter τ and the regularity parameter γ is known. Once the covariance $Q_{\gamma,\tau}$ is constructed we discretize (3.3) using a finite differences (FD) discretization scheme with a pixel size of $2/N_s$, where N_s is the number of detector pixels. We propose two methods to draw samples from $Q_{\gamma,\tau}$.

In the first approach we consider periodic boundary conditions on the box centered at the origin with the size 2-by-2. Note that $Q_{\gamma,\tau}$ is defined via its Fourier transform. Therefore, this choice of boundary conditions allows efficient sampling from $Q_{\gamma,\tau}$ using the fast Fourier transform. For a sample $\xi \sim Q_{\gamma,\tau}$ we assemble $\hat{\xi}$ in the Fourier space. We then use inverse fast Fourier transform (IFFT) to obtain ξ_{ex} . To Ensure that ξ is only valid in D we define $\xi := \xi_{\text{ex}}|_D$. The image α is then constructed using the map $F_{\text{ls}}[\xi]$ for fixed $a^+, a^- \geq 0$. This method allows efficient generation of Gaussian samples.

An alternative, but significantly more expensive, method to sample from $Q_{\gamma,\tau}$ is to numerically compute the eigen-decomposition of $Q_{\gamma,\tau}$. We consider homogeneous Dirichlet boundary conditions and discretize $Q_{\gamma,\tau}$ with the FD method to obtain the matrix M . The Dirichlet boundary conditions ensures that the inclusions appear far from the boundary. We use numerical methods to compute the eigen-decomposition $\{e_i, \lambda_i\}_{i=1}^{N_{\text{KL}}}$ of M . The extraction can be carried out only once for a set of hyperparameters τ and γ . The image α is then construct by directly computing the KL expansion in (3.2) and using the map $F_{\text{ls}}[\xi]$ for fixed $a^+, a^- \geq 0$. Although the Dirichlet boundary conditions are the physically appropriate choice, the direct computation of eigen-decomposition can be challenging when M is severely ill-conditioned. Therefore, in our numerical experiments we only used the first approach.

We construct the posterior measure μ^y and explore it by using the preconditioned Crank-Nicolson (pCN) method [10], which is introduced in Appendix C in detail. The algorithm of Stage 1 is given in Algorithm 4.1.

To show the performance of our method in Stage 1, we consider two types of mean for the density field suggested in [16]. The first mean is computed on the space H and then push-forward to the density space using the map F_{ls} , i.e. $\bar{\alpha} = F_{\text{ls}}[\mathbb{E}\xi]$. This mean conserves the piecewise constant nature of the density field. The other type is the sample mean in the density field, i.e. $\hat{\alpha} = \mathbb{E}F_{\text{ls}}[\xi]$. This mean does not

Algorithm 4.1 Detecting inclusion centers

-
- 1: Construct the posterior measure μ^y using the level set prior for an observation vector y .
 - 2: Draw samples $\{\xi^{(j)}\}_{j=1}^{N_{\text{sample}}}$ by using pCN with [Algorithm C.1](#).
 - 3: Compute $\bar{\alpha} = F_{\text{ls}}[\mathbb{E}\xi]$.
 - 4: Estimate N_{inc} and $\{c_i\}_{i=1}^{N_{\text{inc}}}$ and bounding boxes $[x_{\min}^i, x_{\max}^i] \times [y_{\min}^i, y_{\max}^i]$ from $\bar{\alpha}$.
-

construct a piece-wise constant nature of the density field but provides an approximate uncertainty estimate on the boundary of the inclusions.

We use $\bar{\alpha} = F_{\text{ls}}[\mathbb{E}\xi]$ to estimate the approximate location of the inclusions. We can use standard matrix/image segmentation methods (e.g. [\[45\]](#)) to identify individual inclusions. This also gives us an estimate of the number of existing inclusions. The center of mass for each inclusions is an approximation of the center for the star-shape inclusions.

Remark 4.1. The center defined in the star-shaped inclusions is, in general, not the center of mass. However, the center is a modeling tool to describe inclusions and does not explicitly appear in most applications.

In [Figure 2](#) we present examples of Stage 1. The true densities are generated randomly using the noisy star-shaped prior [\(3.11\)](#). The parallel beam geometry described in [Section 2](#) is used for forward calculations. We set $\theta_{\max} = 180^\circ$, $N_\theta = 100$, and $N_s = 100$ for a full set of images. The sensor length is set to 2 and centered at the origin, thus, the size of the detector pixel is $2/N_s$. The number of inclusions is unknown to the first stage.

[Table 1](#) presents the estimated centers of mass against the star-shaped centers in [Figures 2a to 2c](#). Note that the predicted center of mass is far from the center assigned to the star-shaped inclusions. On the other hand we notice that this estimate is an accurate estimate for the true center of mass of the inclusions. We report that the method consistently had similar results for other examples tested by the authors.

TABLE 1
Prediction of centers

	inclusion # 1	inclusion # 2	inclusion # 3
star-shaped centers	(−0.298, 0.452)	(−0.157, −0.143)	(0.382, −0.252)
exact centers of mass	(−0.279, 0.548)	(−0.139, −0.058)	(0.424, −0.305)
predicted centers of mass	(−0.272, 0.540)	(−0.137, −0.059)	(0.424, −0.300)

We notice that if assumption (III) in [Subsection 3.2.2](#) is satisfied the inclusions are well approximated. In [Figures 2d to 2f](#) we see that $F_{\text{ls}}[\mathbb{E}\xi]$ is falsely identifying the two close inclusions as one. However, [Figure 2f](#) suggests that there is uncertainty in detecting the inclusions and can be interpreted as the violation of assumption (III).

We assign a bounding box $[x_{\min}^i, x_{\max}^i] \times [y_{\min}^i, y_{\max}^i]$, $i = 1, \dots, N_{\text{inc}}$, for each inclusion. We estimate x_{\min}^i by first finding $\bar{x}_{\min}^i = \inf_x \{(x, y) \in \text{ith inclusion in } \bar{\alpha}\}$ and then defining $x_{\min}^i := \bar{x}_{\min}^i - d_{\min}^D/2$, where d_{\min}^D is defined in [Subsection 3.2.2](#) assumption (III). Similarly we can define x_{\max}^i, y_{\min}^i and y_{\max}^i . These bounding boxes are essential for the second stage since it decomposes the domain into regions with a single inclusion. [Remark 3.5](#) ensures that there is a well-defined posterior distribution on such regions for the star-shaped prior.

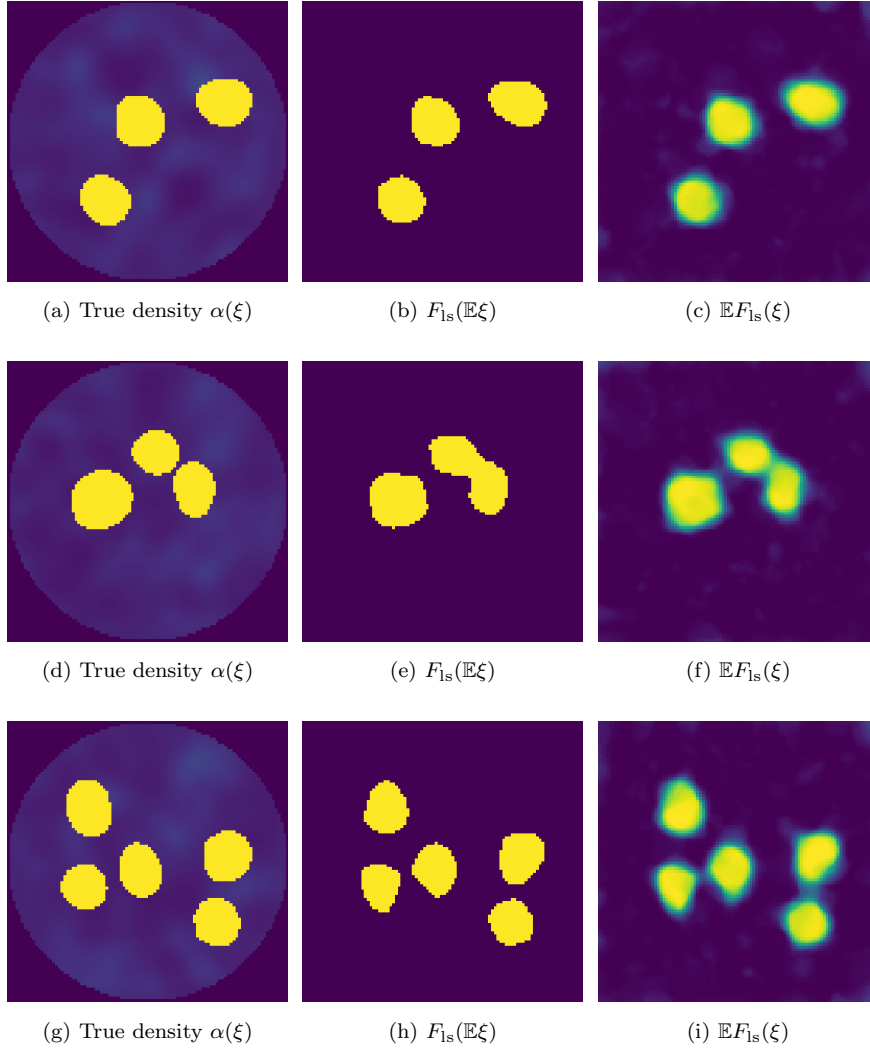


FIG. 2. Example of the first stage in identifying the location of the inclusions. Each row corresponds to the same random variable ξ . First column: the true density. Second column: average sample on parameter space. Third column: average sample on density space.

4.2. Stage Two: Estimation and Uncertainty Quantification of the Boundaries of Inclusions. In this stage we construct the posterior measure μ^y using the star-shaped prior. The number of inclusions N_{inc} is estimated from the previous stage together with the bounding boxes that decompose the domain into regions with a single inclusion. We let ξ_i , for $i = 1, \dots, N_{\text{inc}}$ be the H -valued random variables with $H = \mathbf{T}([0, 2\pi))$.

We assume that the correlation parameter $\tau = 1$ and γ is known in (3.3). This choice of τ indicates that points on the boundary are highly correlation. Since ξ_i are modelling the boundary of the inclusions we may use the periodic boundary conditions to construct $Q_{\gamma,1}$. Furthermore, since ξ_i are 1D we can assemble them directly from (3.4). Furthermore, we assume a constant and known mean function m , in (3.2), for

all ξ_i . The centers for the star-shaped inclusions are taken from the estimated bounds provided in Stage 1.

The posterior measure μ^y is constructed following [Subsection 3.3](#). We draw samples from the posterior distribution using the Gibbs sampling method, which is introduced in [Appendix C](#), to estimate the two types of mean for the posterior, i.e. $\bar{\alpha}_{\mathbb{E}c} = F_{\text{star}}[(\mathbb{E}\xi_i, \mathbb{E}c_i)]$ and $\hat{\alpha}_{\mathbb{E}c} = \mathbb{E}F_{\text{ls}}[(\xi_i, c_i)]$, introduced in [Subsection 4.1](#). Here, the subscript $\mathbb{E}c$ means that the expected image is drawn around the expected centers.

To construct a confidence interval for the boundary of inclusions, we estimate the variance of the random variables ξ_i , $i = 1, \dots, N_{\text{inc}}$. This variance can be computed for each random variable ξ_i in the sample space, i.e. $\text{Var } \xi_i = \mathbb{E}\|\xi_i - \mathbb{E}\xi_i\|_H^2$. Alternatively it can be evaluated point-wise for a selected number of angels $\{\vartheta_j\}_{j=1}^{N_{\text{ang}}}$ in the density field, i.e. $\text{Var } F_{\text{star}}[\xi_i(\vartheta_j)] = \mathbb{E}\|F_{\text{star}}[\xi_i(\vartheta_j)] - \mathbb{E}F_{\text{star}}[\xi_i](\vartheta_j)\|_2^2$. We construct radial confidence band by interpolating the radial confidence intervals for each inclusion. The Algorithm of Stage 2 is given as follows.

Algorithm 4.2 Prediction and uncertainty quantification of the boundary of inclusions

- 1: Input N_{inc} , $\{c_i\}_{i=1}^{N_{\text{inc}}}$ and $[x_{\min}^i, x_{\max}^i] \times [y_{\min}^i, y_{\max}^i]$ obtained by using [Algorithm 4.1](#).
 - 2: **for** $i = 1, \dots, N_{\text{inc}}$ **do**
 - 3: Construct the posterior measure μ^y using the star-shaped prior with single inclusion.
 - 4: Draw samples $\{(\xi_i^{(j)}, c_i^{(j)})\}_{j=1}^{N_{\text{sample}}}$ by using the Gibbs sampling method with [Algorithm C.2](#).
 - 5: **end for**
 - 6: Choose $\{\vartheta_k\}_{k=1}^{N_{\text{ang}}}$ and compute the posterior mean $\mathbb{E}F_{\text{star}}[\xi_1(\vartheta_k)], \dots, \mathbb{E}F_{\text{star}}[\xi_{N_{\text{inc}}}(\vartheta_k)]$.
 - 7: Compute $\text{Var}F_{\text{star}}[\xi_1(\vartheta_k)], \dots, \text{Var}F_{\text{star}}[\xi_{N_{\text{inc}}}(\vartheta_k)]$ to construct radial confidence intervals.
 - 8: Construct uncertainty bands using interpolation.
-

Note that the samples from the radial random variables ξ_i are generally couple with the samples of the centers c_i , due to the structure of the Gibbs sampler. However, by ignoring the center c component of the samples we can approximately achieve independent samples of ξ . We plot the confidence band with respect to the expected center $\mathbb{E}c_i$, for $i = 1, \dots, N_{\text{inc}}$. This is only for illustration purposes and should not be confused with samples of the random variable $\xi|(c = \mathbb{E}c)$. Therefore, the confidence band is a tool to compare uncertainty from one angle ϑ_i to another ϑ_j , $i, j \neq N_{\text{ang}}$ and is not a representation of physical uncertainty in the image.

Remark 4.2. The set of angles $\{\vartheta_j\}_{j=1}^{N_{\text{ang}}}$ is a null-set in $[0, 2\pi)$ with respect to the Lebesgue measure. Therefore the uncertainty band is an indication of local uncertainties. To quantify the global error (the uncertainty in predicting the overall shape of the inclusion) we compute the uncertainty in H or $L^2(D)$, e.g. using the variance $\text{Var}\xi_i = \mathbb{E}\|\xi_i - \mathbb{E}\xi_i\|_H^2$. We can then compare the point-wise error estimate with the global one.

5. Numerical Results. In this section we test the presented method on synthetic images with inclusions. Test images contain single and multiple inclusions with boundaries with various regularities. We also test the method on a tomographic X-ray

data of a lotus root filled with attenuating objects.

5.1. Generated Inclusions. In this section, we consider synthetic images with inclusions. We construct an image (density field α) using the star-shaped prior. We then apply the 2-stage method to estimate the center of inclusions and quantify the uncertainty in predicting the boundaries.

We consider the domain D to be the unit disk. We construct the random density fields using the noisy star-shaped prior (3.11)

$$(5.1) \quad \alpha^{\text{noisy}}(x) = F_{\text{star}}^{\text{noisy}}[\xi_0, (\xi_i, c_i)](x),$$

where foreground and background attenuation is set to $a^+ = 1$ and $a^- = 0.1$, respectively. Recall that ξ_0 is the random variable that controls the fluctuations in the background while ξ_i determines the boundary of a single inclusion. We draw samples from the noisy star-shaped density by first randomly choosing a center in the unit disk and then taking $\xi_0 \sim \mathcal{N}(0, C_{\gamma^0, \tau^0}^0)$ and $\xi_1 \sim \mathcal{N}(0, C_{\gamma^1, \tau^1}^1)$, with $\gamma^0 = 2.5$, $\tau^0 = 50$ as the parameters for the background. We use a sampling-and-elimination method to ensure that the inclusion appears inside the unit disk. We truncate the KL expansion after 100 terms.

In the following sections use the scikit-image package [42], version 0.19.0.dev0, a Python image processing toolkit, to carry out the forward calculations, i.e., 2D Radon transforms from images. The package uses the parallel beam geometry described in Section 2. We set $\theta_{\max} = 180^\circ$ and $N_\theta = 100$ for a full set of images. The sensor length is set to 2 and centered at the origin. This means that L_θ^\perp is centered at the origin and $s \in [-1, 1]$ (see Figure 1).

We apply the first stage of the method following Algorithm 4.1 to estimate the center for the inclusion and the bounding box for where the true center lies. We then use the Gibbs sampler presented in Algorithm C.2 to sample from the posterior measure μ^y . The step sizes \mathbf{b}_1 and \mathbf{b}_2 are chosen such that each component of the Gibbs sampler provides an acceptance rate of 15% to 25%. We collect 10^4 samples from μ^y with an addition of 10^3 samples in a burn-in stage, i.e. samples which do not contribute to the statistics.

We use the variance in the samples to estimate the uncertainties in detecting the boundary of the inclusion. We use the batched mean method presented in Appendix C estimate the variance of the estimated boundary. We take the batch size to be $N_{\text{batch}} = 20$. Recall that we consider two types of variances. The global variance is computed in the sample space as $\mathbb{E}\|\xi - \mathbb{E}\xi\|_H^2$. The local variance is carried on a single point on the boundary in the density space, $\mathbb{E}\|\xi(\vartheta^*) - \mathbb{E}\xi(\vartheta^*)\|_2^2$. A periodic interpolation then results in a radial band of uncertainty.

5.1.1. Single Inclusion. In this section we consider density fields α with a single inclusion. We investigate the effect of the strength of the observation noise on the predictions of the method. The boundary of the inclusion is predicted and the uncertainty in prediction is visualized. The results in this section are illustrated on randomly generated test examples. The authors found similar results for all other test examples with same setting.

To create ground truth images we set $\gamma^1 \in \{1.5, 2, 3\}$, and $\tau^1 = 1$. The true random variables ξ_0 and ξ_1 will remain unknown to the method. We define the *signal to noise ration (SNR)* in an observation to be

$$(5.2) \quad \text{SNR} = \frac{\|y\|_2}{\|\varepsilon\|_2},$$

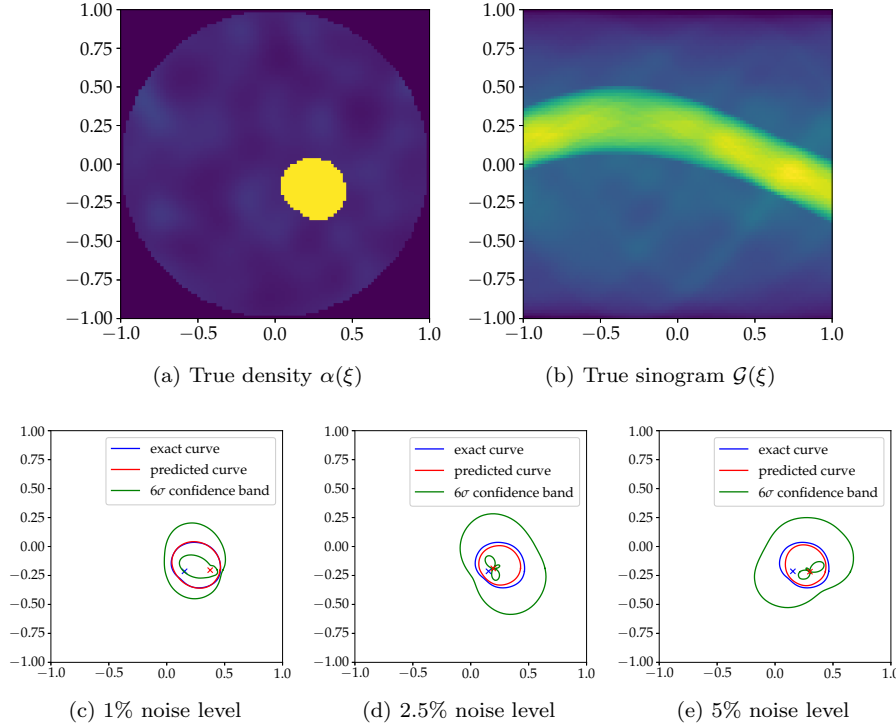


FIG. 3. Illustration of the uncertainty in detecting the boundary of a single inclusion with regularity parameter $\gamma^1 = 3$. Top images represent the true image and the noise-free sinogram. The bottom images represent the output of the method for noise levels 1%, 2.5%, and 5%, respectively. The blue curve and the blue cross represent the exact boundary and the exact star-shaped center. The red cross and the red curve represent $\mathbb{E}c_1$ and $F_{\text{star}}[(\mathbb{E}\xi_1, \mathbb{E}c_1)]$, respectively. The green band indicates the 6σ uncertainty band in the shape of the inclusion.

and define the *noise level* percentage in an observation to be $1/\text{SNR} \times 100$.

Figure 3 shows the performance of the method for a single inclusion with the regularity parameter set to $\gamma^1 = 3$ and noise levels set to 1%, 2.5%, and 5%. We report that the true center of the inclusion is $c = (0.154, -0.215)$. The estimate for the star-shaped center using Algorithm C.2 is $\mathbb{E}c = (0.376, -0.203)$, $\mathbb{E}c = (0.195 - 0.190)$, and, $\mathbb{E}c = (0.302 - 0.216)$, for Figures 3c to 3e, respectively. The estimated centers are illustrated with a red cross.

We notice that the estimated centers are far from the true centers, however, a higher accuracy is observed in the second component of the center compared to the other component. We report the authors found a better match between the true and estimated centers for inclusions with lower regularity parameter γ^1 . We remind that the center for the inclusion is a modeling tool and the goal of the method is to estimate the boundary of the inclusion.

The red curves in Figures 3c to 3e indicate $F_{\text{star}}[(\mathbb{E}\xi_1, \mathbb{E}c_1)]$. In words, this curve presents the estimated boundary of the inclusion illustrated on $\mathbb{E}c$ as the center of inclusion. We notice that all curves present an accurate representation of the boundary of the inclusion. Furthermore, the accuracy of prediction increases as the noise level is reduced. As the estimated centers are far from the true centers, we conclude that the location of the centers are not necessarily unique (The discretization of the true

image before forward calculations can be one explanation for non-uniqueness of the center, but requires further investigation).

We present estimated global variances in Table 2. We notice that the relative difference in variance among the test cases confirms the uncertainty that is visualized in Figure 3. This confirms our intuition that larger observation noise results in larger uncertainty in our prediction.

TABLE 2
Estimation of the variance of the shape

	Figure 3c	Figure 3d	Figure 3e
$\mathbb{E}\ \xi_1 - \mathbb{E}\xi_1\ _H^2$	0.048	0.323	0.334

The green curves in Figures 3c to 3e indicates the 6σ band of uncertainty in predicting the boundary of the inclusion. We evaluate ξ_1 point-wise for angles $\{\theta_j\}_{j=1}^{n_{ang}}$. We then estimate $\text{Var}F_{\text{star}}[\xi_1(\vartheta_j)]$ to compute point-wise uncertainty quantification. We then interpolate the radial confidence intervals to construct the uncertainty band around the boundary of the inclusion.

We notice that the uncertainty band in all test cases completely covers the true outline of the inclusions. It is seen that the uncertainty band is significantly smaller for the test cases with smaller level of observation noise. Although the approximation of the center increases the uncertainty in predicting the boundary, the uncertainty band well covers the true outline of the inclusions.

The confidence band does not provide a uniform uncertainty around the boundary, as it is suggested in Figures 3c to 3e. The variation in the uncertainty around the boundary is a result of the estimated center and the choice of basis functions in the Matérn field.

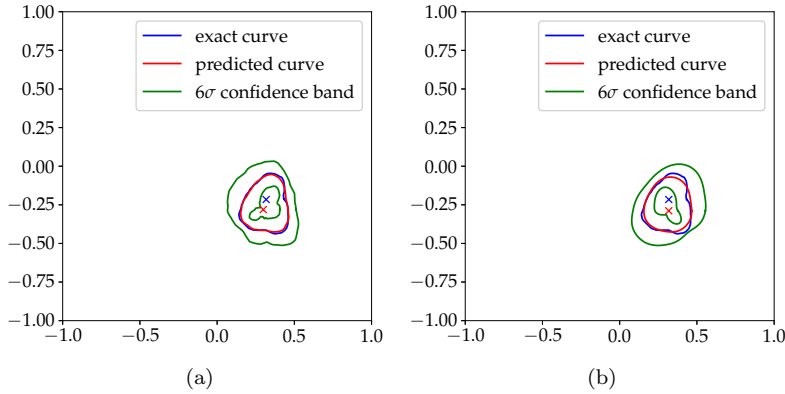


FIG. 4. Illustration of the uncertainty in detecting the boundary where a wrong value for the regularity is used. The ground truth image is constructed with the regularity parameter $\gamma^1 = 2$. (left) the regularity parameter is set to $\gamma^1 = 2$ in the method (right) the regularity parameter is set to $\gamma^1 = 3$ in the method. The blue curve and the blue cross represent the exact boundary and the exact star-shaped center. The red cross and the red curve represent $\mathbb{E}c_1$ and $F_{\text{star}}[\mathbb{E}\xi_1, \mathbb{E}c_1]$, respectively. The green band indicates the 6σ uncertainty band in the shape of the inclusion.

Figure 4 illustrates the case where the regularity parameter γ^1 is miss-evaluated. We generate the ground truth image using $\gamma^1 = 2$. However, in the method we set $\gamma^1 = 3$, a higher value than the true regularity. We then compare the results with the

case were γ^1 is correctly set in the method.

Figure 4a presents detection of a single inclusions when the correct regularity $\gamma^1 = 2$ is used. The estimated curve in Figure 4a accurately represents the true boundary. The location of some of the larger indentations in boundary is also represented in the estimated boundary. Furthermore, we notice that the location of the center of the inclusion is predicted accurately. The 6σ confidence band (the green line) provide the uncertainty around the boundary. We notice a higher uncertainty around the indentations of the true boundary.

In Figure 4b the ground truth image is taken identical to Figure 4a with regularity $\gamma^1 = 2$. However, the method takes $\gamma^1 = 3$ as a prior input. The estimated curve (red curve) provided by the method is a smooth approximation of the true curve. Furthermore it fairly estimates the overall shape and orientation of the inclusion. We notice that the uncertainty band around the boundary is wider than the one in Figure 4a.

We report the global variance of the test cases in Figures 4a and 4b in Table 3. The relative differences between the variances verifies the uncertainty bands indicated in the figures. In addition we note that the global variance in Figure 4b is significantly larger than the one in Figure 4a. This can potentially be used to identify the correct regularity in case γ^1 is also unknown. One approach can be to minimize the global variance over γ^1 . This is left as future work.

TABLE 3
Estimation of the variance

	Figure 4a	Figure 4b
$\mathbb{E}\ \xi_1 - \mathbb{E}\xi_1\ _H^2$	0.0561	0.198

5.2. Multiple Inclusions. In this section we consider density fields α that contains multiple inclusions. We construct the ground truth density fields using the noisy star-shaped prior (3.11) as

$$(5.3) \quad \alpha^{\text{noisy}}(x) = F_{\text{star}}^{\text{noisy}}[\xi_0, \xi_1, \dots, \xi_{N_{\text{inc}}}](x),$$

with $N_{\text{inc}} = 3$. We let $\xi_0 \sim \mathcal{N}(0, C_{\gamma^0, \tau^0}^0)$ and $\xi_i \sim \mathcal{N}(0, C_{\gamma^i, \tau^i}^0)$, for $i = 1, \dots, N_{\text{inc}}$, where $\gamma^0 = 2.5$, $\tau^0 = 50$, $\gamma^i = 3$, and $\tau^i = 1$. Therefore, we expect the inclusions to contain smooth boundaries. Drawing samples from $\alpha^{\text{noisy}}(x)$ requires sampling-and-elimination step to ensure that inclusions are inside the domain and that they do not collide. We truncate the KL expansion for ξ_0 after 200 terms and for ξ_i , $i = 1, \dots, N_{\text{inc}}$, after 100 terms. The noise term ε with noise-level of 1% is considered to construct an observation vector. We collect 10^4 samples from the posterior distribution with an addition of 10^3 samples in the burn-in stage. We report that the authors found similar approximation of the centers for this test case compared to those presented in Subsection 5.1.1 and Subsection 4.1.

Figure 5b shows the ground truth image with three inclusions with Figure 5a the corresponding sinogram. We apply the 2-stage method to estimate the location and the bounds for the centers of inclusions. We then run the Gibbs sampler according to Algorithm 4.2 using parallel computation for each inclusions.

The estimated boundaries are presented in Figure 5c. We notice the centers of all inclusions are estimated with high accuracy. Furthermore, the posterior mean for the boundary of the inclusion provides a precise estimate for the true boundaries. Note that the true inclusions have different size, shape and orientation (e.g. one of the

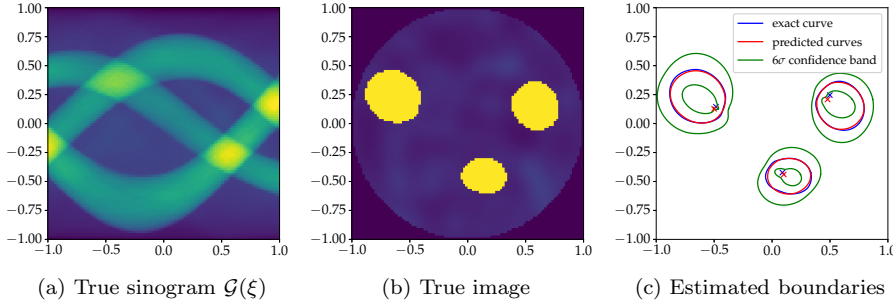


FIG. 5. Illustration of the uncertainty in detecting the boundary for an image with multiple inclusions. (a) noise-free sinogram (b) ground truth image (c) predicted boundaries. The blue curves and the blue crosses represent the exact boundaries and the exact star-shaped centers. The red crosses and the red curves represent $\mathbb{E}c_i$ and $F_{star}[\mathbb{E}\xi_i, \mathbb{E}c_i]$, respectively for $i = 1, 2, 3$. The green bands indicate the 6σ uncertainty band in the shape of the inclusion.

inclusions is more elongated). Although the prior distribution is set identical for all inclusions, the method can find such subtle differences automatically.

We can see global variance of ξ_i , $i = 1, 2, 3$, in Table 4. The uncertainty band illustrated in Figure 5c is compatible with the estimated global variances. We report that the authors find similar results for images with at most 5 inclusions. Given a good initial guess provided from the first stage of the method, we expect the method to perform as well for any number of inclusions.

TABLE 4
Estimation of centers and variances

Inclusion number	Figure 5c		
	$i = 1$	$i = 2$	$i = 3$
True centers	$(-0.484, 0.146)$	$(0.499, 0.246)$	$(0.090, -0.423)$
Estimated centers	$(-0.500, 0.128)$	$(0.480, 0.209)$	$(0.101, -0.439)$
Variance in ξ_i	0.083	0.050	0.065

5.3. Sparse and limited angle imaging. In this section we estimate the boundary of a single inclusion in a sparse angle imaging configuration. We compare imaging setup where the number of angles is $N_\theta = 10$ (compared to $N_\theta = 100$ in Subsections 5.1.1 and 5.2) and we set maximum angle of imaging to be $\theta_{\max} \in \{180^\circ, 90^\circ, 45^\circ\}$. The interval $[0, \theta_{\max})$ is uniformly discretized into imaging angles θ_j , $j = 1, \dots, N_\theta$. In case of limited angle imaging, we indicate theses angles by the normal vector to L_θ^\perp , see Figure 1, in Figures 6d and 6f. The regularity of the inclusion is chosen to be $\gamma^1 = 2.5$. The rest of the parameters for the forward problem and the sampling methods are chosen identical to Subsection 5.1.

The ground truth density field α in this test case is generated randomly using the noisy star-shaped prior. We take a trial and error approach to ensure that the inclusion lies within the unit disk. To understand the effect of the sparsity and imaging angles on predictions, we compare the results to the case where a full set of images ($N_\theta = 100$) is available and to the case where the true center of the inclusion is known.

Figures 6a to 6f shows the test case where the center of the inclusion is fixed to the true star-shaped center. While in Figures 6d to 6f the results regarding the sparse imaging, the first row in Figure 6 uses the full set of images. The width of

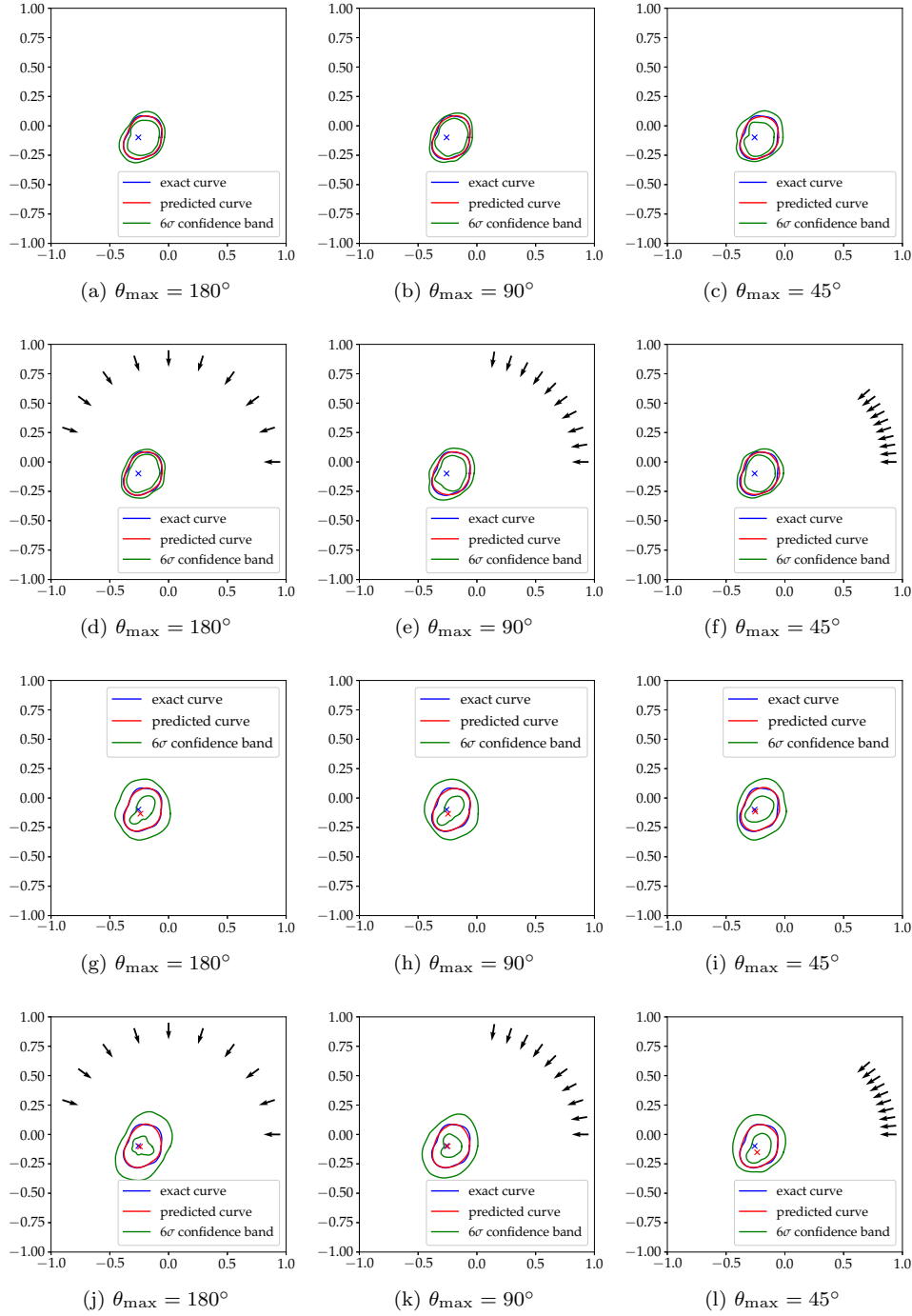


FIG. 6. Example of predicting the boundary of a single inclusion with sparse and limited angle imaging. The imaging points are only illustrated for the sparse imaging cases. The blue curves and the blue crosses represent the exact boundary and the exact star-shaped centers. The red crosses and the red curves represent $\mathbb{E}\xi_1$ and $F_{\text{star}}[\mathbb{E}\xi_1, \mathbb{E}\xi_1]$, respectively. The green bands indicate the 6σ uncertainty band in the shape of the inclusion.

the uncertainty band in Figures 6a and 6d is uniformly distributed the boundary of the inclusion. However, as we move to the right in Figure 6 (as the view angle becomes more limited), prediction of parts of the inclusion becomes more uncertain (the width of the uncertainty band increases). Furthermore, as we move from top to bottom (from Figures 6a to 6c to Figures 6d to 6f), the width of the uncertainty band increases as well. This confirms our intuition that increasing the number of angles in the CT problem reduces the uncertainty in our prediction.

We show the test case with an unknown center for the star-shaped inclusion in Figures 6g to 6l. We notice that the uncertainty in the prediction of the boundary of the inclusion is significantly larger than the previous test cases. As we move from left to right, we cannot notice a qualitative difference in the amount of uncertainty in the predicted boundary.

We notice the increase in the width of the uncertainty band as we move from Figures 6g to 6i to Figures 6j to 6l. Therefore, the method is significantly more sensitive to the number of observations than the number of imaging angle.

We remark that in all test cases in this section the posterior mean provides an excellent approximation for the true boundary and for the true center of the star-shaped inclusion. Furthermore, we report that the overall behavior of the global variances were comparable with the uncertainty presented in Figure 6 as seen in Table 5.

TABLE 5
Estimation of the variance of the shape

	Figure 6g	Figure 6h	Figure 6i	Figure 6j	Figure 6k	Figure 6l
$\mathbb{E}\ \xi_1 - \mathbb{E}\xi_1\ _H^2$	0.0538	0.0485	0.0312	0.0571	0.0493	0.0320

5.4. Lotus Root. In this section we apply our method on a tomographic X-ray data of a lotus root filled with attenuating objects. The data is part of the Finnish inverse problems society (FIPS) open data sets [3, 4]. The data set consists of the X-ray sinogram of a single 2D slice of the lotus root. The sinogram was obtained from a measured 360-projection fanbeam sinogram by down-sampling and taking logarithms. The original (measured) sinogram is also provided in its original form and resolution.

The lotus root has the texture of a potato, presents many holes of different sizes and it is mainly composed of starch (sugar). The structure of the lotus root makes it ideally suitable to stuff it with other objects. The object which is of interest in this experiment is a piece of circular chalk (made of calcium) placed inside the lotus root. The sinogram and the reconstructed image using the filtered back-projection is found in Figure 7c and Figure 7a, respectively. In this example we take Figure 7a as the ground truth image and apply our own forward map to construct the sinogram.

The forward map is constructed using 100 projections with projection angles uniformly distributed in the interval $[0, 180^\circ]$. We assume a Gaussian observation noise $\varepsilon \sim \mathcal{N}(0, \sigma_n^2)$ with 1% noise level.

We set the foreground attenuation to be $a^+ = 0.025$ and the background attenuation to be $a^- = 0.001$. In the first step of the method we set the correlation length for the Matérn-Whittle field to be $\ell = 0.02$ and the regularity parameter $\gamma = 3$. We assume that the observation noise has 1% noise level. The rest of the modelling parameters are chosen identical to the previous subsection. The estimated center for the chalk is found to be $c = (0.055, 0.474)$. We report that the exact center of the chalk is not known.

The estimated curve for the circular chalk is presented in Figure 7b. We note that the image behind the curve estimation is presented as a visualization aid. Our method does not provide a reconstructed image for the whole domain. We notice that the curve precisely follows the outline of the circular chalk. Furthermore the estimated center appears approximately at the center of the inclusion. We report that a star-shaped inclusion with a perfect circular boundary has the center exactly at the middle.

The uncertainty band around the boundary of the inclusion suggests that the reconstruction is an accurate one. We notice an un-even certainty band around the boundary of the inclusion.

To sum, the method provides an excellent reconstruction of the circular inclusion and provides a reliable tool to quantify the uncertainty in the prediction.

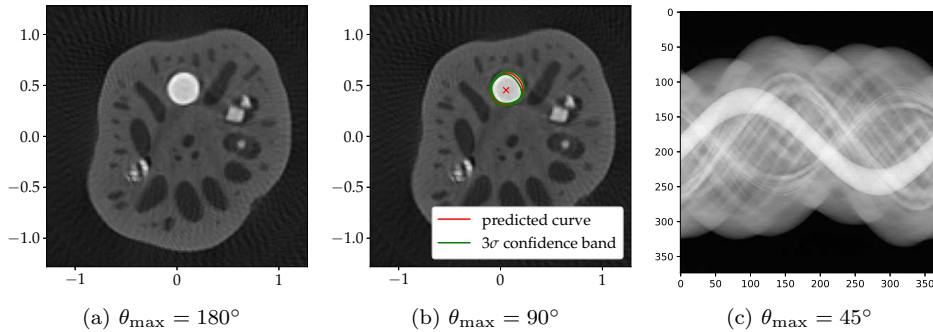


FIG. 7. Prediction of the boundary of a circular chalk in a 2d slice of a lotus root. The red cross and the red curve represent \mathbb{E}_{C_1} and $F_{star}[\mathbb{E}_{\xi_1}, \mathbb{E}_{C_1}]$, respectively. The green band indicates the 3σ uncertainty band in the shape of the inclusion.

6. Conclusions. This work presents an infinite dimensional Bayesian framework for the X-ray CT problem for estimation and uncertainty quantification of inclusion boundaries. The presented method identifies the boundaries of objects with constant attenuation that can be represented as a star-shaped inclusion on a smoothly varying background. Furthermore, we provide a certainty band around the boundary of the object. The method is carried out in two stages. In the first stage we identify approximate location of the inclusions by sampling the posterior constructed with the level set prior. This stage decomposes the image into regions with only a single inclusion. The second stage comprises sampling from the posterior distribution constructed using the star-shaped prior. The decomposition of the image in the first stage guarantees that sampling methods collect samples from the correct distribution of the inclusion boundaries.

The numerical results show that the posterior mean provides an accurate representation of the inclusion boundaries for a wide range of regularities of the boundary. Furthermore, the method consistently performs well in detecting inclusions in challenging X-ray CT scenarios (e.g. for sparse and limited angle imaging). Applying the method on a real data, the tomographic X-ray data of a lotus root filled with a circular chalk, suggest that this method can be extended to real world applications.

The method provided in this work is an accurate method in identifying discontinuities between interfaces in the context of X-ray CT.

Appendix A. More on The Matérn-Whittle Covariance. Recall $D \subset \mathbb{R}^2$

is a bounded region with Lipschitz boundary. We take $H = L^2(D)$. The covariance function of two points $x, y \in D$ for the Matérn-Whittle distribution [33, 22] is given by

$$(A.1) \quad q_{\sigma, \nu, \ell}(x, y) = \sigma^2 \frac{2^{1-\nu}}{\Gamma(\nu)} \left(\frac{\|x - y\|_2}{\ell} \right)^\nu K_\nu \left(\frac{\|x - y\|_2}{\ell} \right).$$

Here, $\|\cdot\|_2$ is the Euclidean norm, $\ell > 0$ is the spatial correlation length, $\nu > 0$ is the smoothness parameter, $\sigma^2 > 0$ is the variance of the value of the field (amplitude scale). Furthermore, K_ν is the modified Bessel function of the second kind of order ν [33, 27].

For $\nu = 1/2$ (A.1) reduces to the exponential covariance $q_{\sigma, 1/2, \ell} = \sigma^2 \exp(-d/\ell)$, with $d = |x - y|$. For larger ν smoothness of $q_{\sigma, \nu, \ell}$ increases. One way to see this is that for $\nu = 1/2 + p$, with $p \in \mathbb{N}^+$, (A.1) can be written as a product of an exponential with a polynomial of order p [1, 33]. Therefore, larger p contributes to higher regularity. As $p \rightarrow \infty$ the polynomial tends to an exponential function and $q_{\sigma, \nu, \ell}$ converges to the squared exponential (Gaussian) covariance function $q_{\sigma, \infty, \ell} = \sigma^2 \exp(-d^2/(2\ell^2))$.

We can construct a discrete density function by discretization D and computing (A.1) for each pair of points. However, this approach result in a full covariance matrix for large correlation length. Inversion of such covariance matrices is challenging for inverse problem applications [35, 27].

An alternative approach is to formulate the covariance as a differential operator of a stochastic partial differential equation (SPDE). A detailed discussion on how to construct this SPDE is beyond the scope of this paper. Below we present a brief sketch of this construction and refer the reader to [35, 49] for a detailed discussion.

The main idea is to construct an H -valued Gaussian random variable ξ from its Fourier expansion. Let ψ be white noise on D , i.e. ψ has zero mean with the covariance operator being the Dirac's delta function $q(x, y) = \delta(\|x - y\|_2)$. Subsequently, all Fourier modes in $\hat{\psi}$ will be present in the Fourier transform of ψ . Furthermore, let $S(w)$ be the Fourier transform of $q_{\sigma, \nu, \ell}/\sigma^2$, known as the *power spectrum*. Now we can define ξ through its Fourier transformation by rescaling $\hat{\psi}$ with $S(w)$ as

$$(A.2) \quad \hat{\xi} := \sigma \sqrt{S(w)} \hat{\psi}.$$

By definition, ξ is a Gaussian random variable distributed according to the covariance function $q_{\sigma, \nu, \ell}$. We recover ξ by applying the inverse Fourier transform to (A.2) and obtain

$$(A.3) \quad \frac{1}{\sqrt{b(\nu)\ell^2}} (I - \ell^2 \Delta)^{(\nu+1)/2} \xi = \psi, \quad b(\nu) = \sigma^2 \frac{4\pi\Gamma(\nu+1)}{\Gamma(\nu)}.$$

Here Δ is the Laplace operator and the covariance operator of ξ corresponding to the covariance function $q_{\sigma, \nu, \ell}$ is given by

$$(A.4) \quad Q_{\sigma, \nu, \ell} = b\ell^2 (I - \ell^2 \Delta)^{-\nu-1}.$$

A simplification of (A.4) is presented in [15, 49] which takes the form

$$(A.5) \quad Q_{\gamma, \tau} = (\tau^2 I - \Delta)^{-\gamma}.$$

Here, $\tau = 1/\ell > 0$ controls the correlation length and $\gamma = \nu + 1$ is the smoothness parameter (see [27] for more detail). For the covariance operator (3.3) to be well

defined we need to impose proper boundary conditions. See [35] for more detail on types of boundary conditions.

Appendix B. Well-posedness of the problem.

DEFINITION B.1. *Let μ_1 and μ_2 be two posterior probability measures defined on $(H, \mathcal{B}(H))$ such that they are both absolutely continuous with respect to the prior measure (μ_0) . The Hellinger distance [31] between μ_1 and μ_2 are given by*

$$(B.1) \quad d_{\text{Hell}}(\mu_1, \mu_2) = \sqrt{\frac{1}{2} \int_H \left| \sqrt{\frac{d\mu_1}{d\mu_0}}(\xi) - \sqrt{\frac{d\mu_2}{d\mu_0}}(\xi) \right|^2 \mu_0(d\xi)}.$$

THEOREM B.2. [12] *Let Φ be the log-likelihood defined (3.12) satisfying assumptions (i)-(iii) in Subsection 3.2.3 and μ_0 be the prior measure defined on $(H, \mathcal{B}(D))$. Furthermore, let $y, y' \in \mathbb{R}^N$ be two observation vector such that $\|y - y'\|_{\Sigma_n} \leq r$, for a fixed $0 \leq r < \infty$. Then we can find $C = C(r) > 0$ such that*

$$(B.2) \quad d_{\text{Hell}}(\mu^y, \mu^{y'}) \leq C \|y - y'\|_{\Sigma_n}.$$

This means that the posterior distribution remains bounded when the observation vector y is perturbed. Hence, the well-posedness of our tomography inverse problem (2.3) with both nonlinear maps F_{ls} and F_{star} are followed directly from this theorem.

Appendix C. Markov Chain Monte Carlo (MCMC) Methods. In this section we briefly introduce the random walk Metropolis-Hastings (RWM) method [34], the preconditioned Crank-Nicolson (pCN) method [10], and the Gibbs sampling method [34]. These methods allow us to sample from the posterior measure μ^y . We choose the pCN method to sample infinite dimensional Gaussian random variables as it is suitable for random variables on function spaces. Furthermore, the convergence rate of this method is independent of the cut off value N_{KL} in (3.2).

Let $f : H \rightarrow \mathbb{R}^k$, be a μ_0 -measurable function. We approximate $\mathbb{E}f$ as the ergodic average

$$(C.1) \quad \mathbb{E}f := \int f \mu_0(d\xi) = \lim_{N_{\text{sample}} \rightarrow \infty} \frac{1}{N_{\text{sample}}} \sum_{i=1}^{N_{\text{sample}}} f(\xi^{(i)}).$$

Here, $\{\xi^{(i)}\}_{i=1}^{N_{\text{sample}}}$ is a Markov chain with a transition kernel \mathbb{K}_y . We refer the reader to [24] for properties of a transition kernel suitable for (C.1).

The aim of an MCMC method is to construct a transition function (a formula to go from $\xi^{(i)}$ to $\xi^{(i+1)}$ in (C.1)) which result in an appropriate transition kernel \mathbb{K}_y . The pCN is an MCMC method suitable for H -valued Gaussian random variables. This method is robust under the resolution of discretization of the random variables. Below we briefly introduce pCN following the notations in [10].

We introduce the pCN to sample from a single Gaussian random variable ξ . Later in this section we discuss how to generalize this to sample from multiple independent Gaussian random variables.

Let μ^y be the posterior measure on a Hilbert space $(H, \langle \cdot, \cdot \rangle)$ and $\mu_0 \sim \mathcal{N}(0, Q)$ be a prior measure. Let $\mathbb{K}(\xi, \cdot)$ be the transition kernel on H and η denote a measure on $H \times H$ such that if $\xi \sim \mu^y$ then $\zeta | \xi \sim \mathbb{K}_y(\xi, \cdot)$. We denote by η^\perp the measure where the roles of ξ and ζ are reversed. If η^\perp is equivalent to η , in the sense of measure,

then the Radon-Nikodym derivative $d\eta^\perp/d\eta$ is well defined and we can define the acceptance probability

$$(C.2) \quad a(\xi, \zeta) = \min \left\{ 1, \frac{d\eta^\perp}{d\eta}(\xi, \zeta) \right\}.$$

This means $\xi^{(i+1)} := \zeta$ with probability $a(\xi^{(i+1)}, \zeta)$ and $\xi^{(i+1)} := \xi$ otherwise.

The standard random walk proposal function results in η^\perp that is singular with respect to η [10] when ξ is an H -valued function. This results in rejecting all proposed moves with probability 1. The pCN proposal function [10] is given by

$$(C.3) \quad \zeta = (1 - \mathbf{b}^2)^{1/2} \xi + \mathbf{b} \varrho,$$

where $\varrho \sim \mathcal{N}(0, Q)$, and $\mathbf{b} \in [0, 1]$. This choice of proposal results in a well defined $d\eta^\perp/d\eta$ given by [10]

$$(C.4) \quad \frac{d\eta^\perp}{d\eta}(\xi, \zeta) = \exp(\eta(\xi, \zeta) - \eta(\zeta, \xi)) = \exp(\Phi(\xi; y) - \Phi(\zeta; y)).$$

We summarize the pCN sampling method in [Algorithm C.1](#).

Algorithm C.1 preconditioned Crank–Nicolson method for collecting N_{samp} samples

- 1: Set $k = 0$ and take the initial sample $\xi^{(0)}$.
 - 2: **for** $k \leq N_{\text{samp}}$ **do**
 - 3: Propose $\zeta = (1 - \mathbf{b}^2)^{1/2} \xi^{(k)} + \mathbf{b} \varrho$, $\varrho \sim \mathcal{N}(0, Q)$.
 - 4: Set $\xi^{(k+1)} = \zeta$ with probability $a(\xi^{(k)}, \zeta)$, defined in (C.2) together with (C.4), and $\xi^{(k+1)} = \xi^{(k)}$ otherwise.
 - 5: $k \leftarrow k + 1$.
 - 6: **end for**
-

Recall that star-shaped prior is defined for the joint random variable (ξ_i, c_i) . To construct an MCMC method to sample from $(\xi_i, c_i)|y$ we use a *Gibbs*-type [34] sampling method. Such methods alternatively sample from the random variables $\xi_i|c_i, y$ and $c_i|\xi_i, y$ and constructed Markov chain $[\xi_i^{(k)}, c_i^{(k)}]_{k=1}^{N_{\text{sample}}}$ contains ergodic properties as in [Equation \(C.1\)](#) [34]. In this paper we construct a Gibbs sampler following the structure:

$$(C.5) \quad \xi_i^{(k+1)} \sim \mathbb{K}_y^{c_i^{(k)}}(\xi_i^{(k)}, \cdot), \quad c_i^{(k+1)} \sim \mathbb{L}_y^{\xi_i^{(k+1)}}(c_i^{(k)}, \cdot).$$

Here, $\mathbb{K}_y^{c_i}$ and $\mathbb{L}_y^{\xi_i}$ are Metropolis-Hastings Markov kernel reversible with respect to $\xi|c, y$ and $c|\xi, y$, respectively. For the random variable $\xi|c, y$ we use a pCN proposal function with the acceptance probability of

$$(C.6) \quad a(\xi, \zeta) = \min\{1, \exp(\Phi((\xi_i, c_i); y) - \Phi(\zeta_0, (\zeta_i, c_i); y))\}.$$

For the random variable $c|\xi, y$ we use the standard random walk MH proposal function with the acceptance probability of

$$(C.7) \quad r(c, o) = \min\{1, \exp(\Phi((\xi_i, c_i); y) - \Phi((\xi_i, o_i); y))\}.$$

Note that we dropped the uniform prior in (C.7) as both c and o are restricted to the same interval. We summarize the Gibbs sampler for μ^y constructed with the star-shaped prior in [Algorithm C.2](#).

Algorithm C.2 The Gibbs sampling method for collecting N_{samp} samples

-
- 1: Set $k = 0$ and take the initial sample $(\xi_i^{(0)}, c_i^{(0)})$.
 - 2: **for** $k \leq N_{\text{samp}}$ **do**
 - 3: Propose $\zeta = (1 - \mathbf{b}_1^2)^{1/2} \xi^{(k)} + \mathbf{b}_1 \varrho$, $\varrho \sim \mathcal{N}(0, Q)$.
 - 4: Set $\xi_i^{(k+1)} = \zeta$ with probability $a(\xi_i^{(k)}, \zeta)$, defined in (C.6), and $\xi_i^{(k+1)} = \xi_i^{(k)}$ otherwise.
 - 5: Propose $o = c_i^{(k)} + \mathbf{b}_2 \rho$, $\rho \sim \mathcal{N}(0, I)$.
 - 6: Set $c_i^{(k+1)} = o$ with probability $r(c_i^{(k)}, o)$, defined in (C.7), and $c_i^{(k+1)} = c_i^{(k)}$ otherwise.
 - 7: $k \leftarrow k + 1$.
 - 8: **end for**
-

We truncate (C.1) and approximate $\mathbb{E}f$ using the estimator

$$(C.8) \quad \mathbb{E}f \approx m_{\text{MCMC}}(f(\xi)) := \frac{1}{N_{\text{sample}}} \sum_{i=1}^{N_{\text{sample}}} f(\xi^{(i)}).$$

And easy way to estimate the error in this approximation is using *batched mean* [34]. We pick an integer l_{batch} and put samples in batches of size l_{batch} such that samples assigned to different batches are almost independent, for most batches. The mean estimator for each batch is $m_{\text{MCMC}}^{(j)}(f)$, for $j = 1, \dots, N_{\text{batches}}$, and are almost independent. Now the variance of $m_{\text{MCMC}}(f)$ takes the form

$$(C.9) \quad \text{Var } m_{\text{MCMC}}(f(\xi)) \approx \frac{\sigma_{\text{batch}}^2}{N_{\text{batch}}}, \quad \sigma_{\text{batch}}^2 = \frac{1}{N_{\text{batch}}^2} \sum_{j=1}^{N_{\text{batch}}} \text{Var } m_{\text{MCMC}}^{(j)}(f(\xi)).$$

Following [34] we use the central limit theorem to construct confidence intervals.

Note that we chose the batch mean method due to its simplicity. A better but computationally much more expensive in constructing confidence intervals is computing the autocorrelation [34] of $f(\xi^{(i)})$ under Markov chain sampling. We refer the reader to [30] for a detailed review of error estimation for MCMC methods.

REFERENCES

- [1] M. ABRAMOWITZ, I. A. STEGUN, AND R. H. ROMER, *Handbook of mathematical functions with formulas, graphs, and mathematical tables*, 1988.
- [2] C. V. ALVINO AND A. J. YEZZI, *Tomographic reconstruction of piecewise smooth images*, in Proceedings of the 2004 IEEE Computer Society Conference on Computer Vision and Pattern Recognition, 2004. CVPR 2004., vol. 1, IEEE, 2004, pp. I–I.
- [3] T. A. BUBBA, A. HAUPTMANN, S. HUOTARI, J. RIMPELÄINEN, AND S. SILTANEN, *Tomographic X-ray data of a lotus root filled with attenuating objects*, Sept. 2016, <https://doi.org/10.5281/zenodo.1254204>, <https://doi.org/10.5281/zenodo.1254204>.
- [4] T. A. BUBBA, A. HAUPTMANN, S. HUOTARI, J. RIMPELÄINEN, AND S. SILTANEN, *Tomographic x-ray data of a lotus root filled with attenuating objects*, 2016, <https://arxiv.org/abs/1609.07299>.
- [5] T. BUI-THANH AND O. GHATTAS, *An analysis of infinite dimensional bayesian inverse shape acoustic scattering and its numerical approximation*, SIAM/ASA Journal on Uncertainty Quantification, 2 (2014), pp. 203–222, <https://doi.org/10.1137/120894877>, <https://doi.org/10.1137/120894877>, <https://arxiv.org/abs/https://doi.org/10.1137/120894877>.
- [6] T. F. CHAN AND L. A. VESE, *Active contours without edges*, IEEE Transactions on image processing, 10 (2001), pp. 266–277.

- [7] C. CHAPDELAINE, A. MOHAMMAD-DJAFARI, N. GAC, AND E. PARRA, *Variational bayesian approach in model-based iterative reconstruction for 3d x-ray computed tomography with gauss-markov-potts prior*, in Multidisciplinary Digital Publishing Institute Proceedings, vol. 33, 2019, p. 4.
- [8] Y. CHEN, D. GAO, C. NIE, L. LUO, W. CHEN, X. YIN, AND Y. LIN, *Bayesian statistical reconstruction for low-dose x-ray computed tomography using an adaptive-weighting nonlocal prior*, Computerized Medical Imaging and Graphics, 33 (2009), pp. 495–500.
- [9] Y.-T. CHEN AND D.-C. TSENG, *Medical image segmentation based on the bayesian level set method*, in Medical Imaging and Informatics, X. Gao, H. Müller, M. J. Loomes, R. Comley, and S. Luo, eds., Berlin, Heidelberg, 2008, Springer Berlin Heidelberg, pp. 25–34.
- [10] S. L. COTTER, G. O. ROBERTS, A. M. STUART, AND D. WHITE, *MCMC methods for functions: Modifying old algorithms to make them faster*, Statistical Science, 28 (2013), <https://doi.org/10.1214/13-sts421>, <https://doi.org/10.1214/13-sts421>.
- [11] V. A. DAHL, A. B. DAHL, AND P. C. HANSEN, *Computing segmentations directly from x-ray projection data via parametric deformable curves*, Measurement Science and Technology, 29 (2017), p. 014003.
- [12] M. DASHTI AND A. M. STUART, *The Bayesian Approach to Inverse Problems*, Springer International Publishing, Cham, 2017, pp. 311–428, https://doi.org/10.1007/978-3-319-12385-1_7, https://doi.org/10.1007/978-3-319-12385-1_7.
- [13] E. DEBREUVE, M. BARLAUD, G. AUBERT, AND J. DARCOURT, *Attenuation map segmentation without reconstruction using a level set method in nuclear medicine imaging*, in Proceedings 1998 International Conference on Image Processing. ICIP98 (Cat. No. 98CB36269), vol. 1, IEEE, 1998, pp. 34–38.
- [14] M. M. DUNLOP, T. HELIN, AND A. M. STUART, *Hyperparameter estimation in bayesian map estimation: Parameterizations and consistency*, The SMAI journal of computational mathematics, 6 (2020), pp. 69–100.
- [15] M. M. DUNLOP, M. A. IGLESIAS, AND A. M. STUART, *Hierarchical bayesian level set inversion*, Statistics and Computing, 27 (2016), pp. 1555–1584, <https://doi.org/10.1007/s11222-016-9704-8>, <https://doi.org/10.1007/s11222-016-9704-8>.
- [16] M. M. DUNLOP AND A. M. STUART, *The bayesian formulation of eit: Analysis and algorithms*, 2016, <https://doi.org/10.3934/ipi.2016030>, <http://aims sciences.org//article/id/d9e2dc77-0da0-4532-95df-b2c6e5a9eece>.
- [17] H. ELHALAWANI, A. S. MOHAMED, A. L. WHITE, J. ZAFEREO, A. J. WONG, J. E. BERENDS, S. ABOHASHIM, B. WILLIAMS, J. M. AYMARD, A. KANWAR, ET AL., *Matched computed tomography segmentation and demographic data for oropharyngeal cancer radiomics challenges*, Scientific data, 4 (2017), p. 170077.
- [18] E. GIBSON, F. GIGANTI, Y. HU, E. BONMATI, S. BANDULA, K. GURUSAMY, B. DAVIDSON, S. P. PEREIRA, M. J. CLARKSON, AND D. C. BARRATT, *Automatic multi-organ segmentation on abdominal ct with dense v-networks*, IEEE transactions on medical imaging, 37 (2018), pp. 1822–1834.
- [19] G. GRIMMETT AND D. STIRZAKER, *Probability and random processes*, vol. 80, Oxford university press, 2001, http://scholar.google.com/scholar.bib?q=info:xzStZXK20NkJ:scholar.google.com/&output=citation&hl=en&as_sdt=0,5&ct=citation&cd=0.
- [20] P. C. HANSEN, J. S. JØRGENSEN, AND W. R. B. LIONHEART, *Computed Tomography: Algorithms, Insight, and Just Enough Theory*, SIAM, to appear.
- [21] J. HUANG, Z. DENG, AND L. XU, *Bayesian approach for inverse interior scattering problems with limited aperture*, Applicable Analysis, (2020), pp. 1–14.
- [22] I. A. IBRAGIMOV AND Y. A. ROZANOV, *Gaussian random processes*, Springer-Verlag New York, 1978.
- [23] M. A. IGLESIAS, Y. LU, AND A. M. STUART, *A bayesian level set method for geometric inverse problems*, arXiv preprint arXiv:1504.00313, (2015).
- [24] J. KAIPIO AND E. SOMERSALO, *Statistical and computational inverse problems*, vol. 160, Springer Science & Business Media, 2006.
- [25] S. L. LASSI ROININEN, JANNE M. J. HUTTUNEN, *Whittle-matérn priors for bayesian statistical inversion with applications in electrical impedance tomography*, Inverse Problems & Imaging, 8 (2014), pp. 561–586.
- [26] O. LEY ET AL., *Lower-bound gradient estimates for first-order hamilton-jacobi equations and applications to the regularity of propagating fronts*, Advances in Differential Equations, 6 (2001), pp. 547–576.
- [27] F. LINDGREN, H. RUE, AND J. LINDSTRÖM, *An explicit link between gaussian fields and gaussian markov random fields: the stochastic partial differential equation approach*, Journal of the Royal Statistical Society: Series B (Statistical Methodology), 73 (2011),

- pp. 423–498, <https://doi.org/10.1111/j.1467-9868.2011.00777.x>, <https://doi.org/10.1111/j.1467-9868.2011.00777.x>.
- [28] S. LIU, J. JIA, Y. D. ZHANG, AND Y. YANG, *Image reconstruction in electrical impedance tomography based on structure-aware sparse bayesian learning*, IEEE transactions on medical imaging, 37 (2018), pp. 2090–2102.
 - [29] F. NATTERER, *The mathematics of computerized tomography*, SIAM, 2001.
 - [30] A. B. OWEN, *Monte Carlo theory, methods and examples*, 2013.
 - [31] L. PARDO, *Statistical inference based on divergence measures*, CRC press, 2018.
 - [32] R. RAMLAU AND W. RING, *A mumford–shah level-set approach for the inversion and segmentation of x-ray tomography data*, Journal of Computational Physics, 221 (2007), pp. 539–557.
 - [33] C. E. RASMUSSEN, *Gaussian processes in machine learning*, in Summer school on machine learning, Springer, 2003, pp. 63–71.
 - [34] C. ROBERT AND G. CASELLA, *Monte Carlo statistical methods*, Springer Science & Business Media, 2013.
 - [35] L. ROININEN, J. M. J. HUTTUNEN, AND S. LASANEN, *Whittle-matérn priors for bayesian statistical inversion with applications in electrical impedance tomography*, Inverse Problems & Imaging, 8 (2014), pp. 561–586, <https://doi.org/10.3934/ipi.2014.8.561>, <https://doi.org/10.3934/ipi.2014.8.561>.
 - [36] A. K. SAIBABA, P. PRASAD, E. DE STURLER, E. MILLER, AND M. E. KILMER, *Randomized approaches to accelerate mcmc algorithms for bayesian inverse problems*, Journal of Computational Physics, 440 (2021), p. 110391, <https://doi.org/https://doi.org/10.1016/j.jcp.2021.110391>, <https://www.sciencedirect.com/science/article/pii/S0021999121002862>.
 - [37] N. B. SMITH AND A. WEBB, *Introduction to Medical Imaging*, Cambridge University Press, 2009, <https://doi.org/10.1017/cbo9780511760976>, <https://doi.org/10.1017/cbo9780511760976>.
 - [38] C. SOUSSEN AND A. MOHAMMAD-DJAFARI, *Polygonal and polyhedral contour reconstruction in computed tomography*, IEEE Transactions on Image Processing, 13 (2004), pp. 1507–1523.
 - [39] S. SULLIVAN, A. NOBLE, AND J. PONCE, *On reconstructing curved object boundaries from sparse sets of x-ray images*, in International Conference on Computer Vision, Virtual Reality, and Robotics in Medicine, Springer, 1995, pp. 385–391.
 - [40] J.-P. THIRION, *Segmentation of tomographic data without image reconstruction*, IEEE transactions on medical imaging, 11 (1992), pp. 102–110.
 - [41] F. URIBE, J. M. BARDSLEY, Y. DONG, P. C. HANSEN, AND N. A. B. RIIS, *A hybrid gibbs sampler for edge-preserving tomographic reconstruction with uncertain view angles*, 2021, <https://arxiv.org/abs/arXiv:2104.06919>.
 - [42] S. VAN DER WALT, J. L. SCHÖNBERGER, J. NUNEZ-IGLESIAS, F. BOULOGNE, J. D. WARNER, N. YAGER, E. GOULLART, AND T. YU, *scikit-image: image processing in python*, PeerJ, 2 (2014), p. e453, <https://doi.org/10.7717/peerj.453>, <https://doi.org/10.7717/peerj.453>.
 - [43] L. WANG, A. MOHAMMAD-DJAFARI, AND N. GAC, *X-ray computed tomography using a sparsity enforcing prior model based on haar transformation in a bayesian framework*, Fundamenta Informaticae, 155 (2017), pp. 449–480.
 - [44] S. WANG, A. CHEN, L. YANG, L. CAI, Y. XIE, J. FUJIMOTO, A. GAZDAR, AND G. XIAO, *Comprehensive analysis of lung cancer pathology images to discover tumor shape and boundary features that predict survival outcome*, Scientific reports, 8 (2018), pp. 1–9.
 - [45] J. R. WEAVER, *Centrosymmetric (cross-symmetric) matrices, their basic properties, eigenvalues, and eigenvectors*, The American Mathematical Monthly, 92 (1985), pp. 711–717, <https://doi.org/10.1080/00029890.1985.11971719>, <https://doi.org/10.1080/00029890.1985.11971719>.
 - [46] A. D. WESTON, P. KORFIATIS, T. L. KLINE, K. A. PHILBRICK, P. KOSTANDY, T. SAKINIS, M. SUGIMOTO, N. TAKAHASHI, AND B. J. ERICKSON, *Automated abdominal segmentation of ct scans for body composition analysis using deep learning*, Radiology, 290 (2019), pp. 669–679.
 - [47] S. YOON, A. R. PINEDA, AND R. FAHRIG, *Level set reconstruction for sparse angularly sampled data*, in 2006 IEEE Nuclear Science Symposium Conference Record, vol. 6, IEEE, 2006, pp. 3420–3423.
 - [48] S. YOON, A. R. PINEDA, AND R. FAHRIG, *Simultaneous segmentation and reconstruction: A level set method approach for limited view computed tomography*, Medical physics, 37 (2010), pp. 2329–2340.
 - [49] H. ZHANG, *Inconsistent estimation and asymptotically equal interpolations in model-based geostatistics*, Journal of the American Statistical Association, 99 (2004), pp. 250–261.